material at uniquely defined locations. Just as messenger RNAs encode the one-dimensional positioning of transfer-RNA adaptors along their lengths, rigid DNA nanostructures could encode the positioning of sequence-specific DNA binders along their three-dimensional frameworks. DNA nanostructures, therefore, can be regarded as devices that use molecular recognition to translate sequence information into three-dimensional positions. The demonstration of a clonable DNA octahedron is a step towards making the translation of DNA sequence information into position more practical and more versatile. □

Methods

Design of sequences

PX sequences were chosen as will be described elsewhere (W.M.S. & G.F.J., manuscript in preparation). DX sequences were chosen arbitrarily, using the model junction J1[18] for the crossover junctions. The DX sequences were examined to eliminate any seven-nucleotide repeats. Folding of the assembled heavy chain was analysed using MFOLD[19]. Iterative changes were made to the sequence until the target branched-tree structure was achieved as the lowest-energy output.

Folding conditions

Folding was achieved by incubation at 90 °C for 5 min, 65 °C for 20 min, 55 °C for 20 min, 45 °C for 20 min, and 37 °C for 30 min. The folding mixture contained 100 nM heavy chain, 400 nM each of the five light chains, 10 mM $MgCl_2$, 50 mM NaCl, and 40 mM EPPS (pH 7.5).

Synthesis, cloning, and purification of single-stranded DNA

The 1,669-nucleotide heavy chain was constructed by polymerase chain reaction (PCR)-based assembly[20], using synthetic oligodeoxynucleotides prepared by standard phosphoramidite chemistry on a PerSeptive Biosystems Expedite 8900 automated DNA synthesizer. The PCR products were gel purified and ligated into pBS II KS$^+$ plasmids, which were transformed into *Escherichia coli* (see Supplementary Information for additional details). Multiple clones were selected and sequenced to identify error-free clones. An *Eco*R V site was placed upstream and an N.*Bbv*C IA (nicking endonuclease) site was placed downstream of the heavy-chain sequence using the Stratagene Quikchange cloning kit. The plasmid was amplified in *E. coli* and purified using the QIAGEN QiaQuick ion-exchange chromatography system. The desired single strand was obtained by excision with *Eco*R V and N.*Bbv*C IA, then purified by electrophoresis in a 1.5% alkaline agarose gel, and further purified by electrophoresis in a 1.5% native agarose gel. The light chains were prepared by chemical synthesis. The sequences of all oligodeoxynucleotides used in this study are provided in the Supplementary Information.

Electron microscopy

Cryo-electron microscopy was performed as described[15]. A 4-μl drop of folded DNA, concentrated to 500 nM by microdialysis, was placed on a 300-mesh copper grid covered with a continuous carbon substrate and glow-discharged in amyl amine. The grid was blotted for ∼2 s with Whatman filter paper no. 1 and plunge-frozen into liquid ethane. The specimen was observed at −176 °C using a Gatan 626 cryo-stage on a Philips Tecnai F20 FEG operating at 120 kV. Paired images at approximately 0.6 and 2.0 μm defocus were recorded on a Tietz 2k × 2k charge-coupled device (CCD) camera under low-dose conditions using the Leginon[21] automated data collection software system. The magnification was ×62,000, resulting in a pixel size of 2.24 Å. The best 961 images of boxed particles at 2.0-μm defocus were used for three-dimensional reconstruction using the program EMAN[22]. For verification, a second set of paired images was collected and used to carry out an independent reconstruction (see Supplementary Information).

An initial model was generated using 120 particles and the EMAN program 'startoct'. This model was used to produce a set of projections with an angular interval of 3°. The images were aligned with these reference projections to determine the origins and orientations, and a three-dimensional reconstruction was calculated. Cycles of angular refinement were performed with an angular interval of 3° until convergence, with a total of 665 particles contributing to the final average map. Full octahedral symmetry was imposed during the reconstruction. To evaluate the quality of the reconstruction, the data were divided into two groups, and two independent reconstructions were calculated. The resolution of the final reconstruction was estimated as 32 Å, where the Fourier shell correlation between the two independent reconstructions started to fall below 0.5. Maps were rendered using the UCSF Chimera package[23].

1. Seeman, N. C. DNA in a material world. *Nature* **421,** 427–431 (2003).
2. Seeman, N. C. DNA nanotechnology: novel DNA constructions. *Annu. Rev. Biophys. Biomol. Struct.* **27,** 225–248 (1998).
3. Wilson, D. S. & Szostak, J. W. *In vitro* selection of functional nucleic acids. *Annu. Rev. Biochem.* **68,** 611–647 (1999).
4. Chen, J. H. & Seeman, N. C. Synthesis from DNA of a molecule with the connectivity of a cube. *Nature* **350,** 631–633 (1991).
5. Zhang, Y. & Seeman, N. C. The construction of a DNA truncated octahedron. *J. Am. Chem. Soc.* **116,** 1661–1669 (1994).
6. Dorenbeck, A.. *DNA Nanostructures by Self-Assembly of Trisoligonucleotidyls.* Thesis, Univ. Bochum (2000).
7. Seeman, N. C. Construction of three-dimensional stick figures from branched DNA. *DNA Cell Biol.* **10,** 475–486 (1991).
8. Seeman, N. C. Nucleic-acid junctions and lattices. *J. Theor. Biol.* **99,** 237–247 (1982).
9. Seeman, N. C. *De novo* design of sequences for nucleic acid structural engineering. *J. Biomol. Struct. Dyn.* **8,** 573–581 (1990).
10. Li, X. J., Yang, X. P., Qi, J. & Seeman, N. C. Antiparallel DNA double crossover molecules as components for nanoconstruction. *J. Am. Chem. Soc.* **118,** 6131–6140 (1996).
11. Larson, S. B. *et al.* Double-helical RNA in satellite tobacco mosaic virus. *Nature* **361,** 179–182 (1993).
12. Tang, L. *et al.* The structure of Pariocoto virus reveals a dodecahedral cage of duplex DNA. *Nature Struct. Biol.* **8,** 77–83 (2001).
13. Zhang, X., Yan, H., Shen, Z. & Seeman, N. C. Paranemic cohesion of topologically-closed DNA molecules. *J. Am. Chem. Soc.* **124,** 12940–12941 (2002).
14. Sa-Ardyen, P., Vologodskii, A. V. & Seeman, N. C. The flexibility of DNA double crossover molecules. *Biophys. J.* **84,** 3829–3837 (2003).
15. Dubochet, J. *et al.* Cryo-electron microscopy of vitrified specimens. *Q. Rev. Biophys.* **21,** 129–228 (1988).
16. Frank, J. Averaging of low exposure electron micrographs of non-periodic objects. *Ultramicroscopy* **1,** 159–162 (1975).
17. Frank, J. Classification of macromolecular assemblies studied as 'single particles'. *Q. Rev. Biophys.* **23,** 281–329 (1990).
18. Seeman, N. C. & Kallenbach, N. R. Design of immobile nucleic acid junctions. *Biophys. J.* **44,** 201–209 (1983).
19. Zuker, M. Mfold web server for nucleic acid folding and hybridization prediction. *Nucleic Acids Res.* **31,** 1–10 (2003).
20. Stemmer, W. P., Crameri, A., Ha, K. D., Brennan, T. M. & Heyneker, H. L. Single-step assembly of a gene and entire plasmid from large numbers of oligodeoxyribonucleotides. *Gene* **64,** 49–53 (1995).
21. Carragher, B. *et al.* Leginon: an automated system for acquisition of images from vitreous ice specimens. *J. Struct. Biol.* **132,** 33–45 (2000).
22. Ludtke, S. J., Baldwin, P. R. & Chiu, W. EMAN: semiautomated software for high-resolution single-particle reconstructions. *J. Struct. Biol.* **128,** 82–97 (1999).
23. Huang, C. C., Couch, G. S., Pettersen, E. F. & Ferrin, T. E. Chimera: an extensible molecular modeling application constructed using standard components. *Pacif. Symp. Biocomput.* **1,** 724 (1996).

....

Earthquake nucleation by transient deformations caused by the M = 7.9 Denali, Alaska, earthquake

J. Gomberg[1], P. Bodin[2], K. Larson[3] & H. Dragert[4]

[1]US Geological Survey, Center for Earthquake Research and Information, 3876 Central Ave. Suite 2, and [2]Center for Earthquake Research and Information, The University of Memphis, 3876 Central Ave. Suite 1, Memphis, Tennessee 38152-3050, USA
[3]Department of Aerospace Engineering Sciences, University of Colorado at Boulder, Boulder, Colorado 80309-0429, USA
[4]Geological Survey of Canada, Pacific Geoscience Centre, 9860 West Saanich Road, Sidney, British Columbia, V8L 4B2, Canada

....

The permanent and dynamic (transient) stress changes inferred to trigger earthquakes are usually orders of magnitude smaller than the stresses relaxed by the earthquakes themselves, implying that triggering occurs on critically stressed faults[1–4]. Triggered seismicity rate increases may therefore be most likely to occur in areas where loading rates are highest and elevated pore pressures,

perhaps facilitated by high-temperature fluids, reduce frictional stresses and promote failure[5–7]. Here we show that the 2002 magnitude $M = 7.9$ Denali, Alaska, earthquake triggered widespread seismicity rate increases throughout British Columbia and into the western United States. Dynamic triggering by seismic waves should be enhanced in directions where rupture directivity focuses radiated energy, and we verify this using seismic and new high-sample GPS recordings of the Denali mainshock. These observations are comparable in scale only to the triggering caused by the 1992 $M = 7.4$ Landers, California, earthquake[1], and demonstrate that Landers triggering did not reflect some peculiarity of the region or the earthquake. However, the rate increases triggered by the Denali earthquake occurred in areas not obviously tectonically active, implying that even in areas of low ambient stressing rates, faults may still be critically

stressed and that dynamic triggering may be ubiquitous and unpredictable.

The Denali earthquake ruptured nearly 300 km of fault, propagating unilaterally southeastwards[8,9] (Fig. 1). The system of faults that broke comprises part of the Pacific–North American plate boundary, which is defined by a series of strike–slip faults that continue through the Alaska Panhandle, the southwestern Yukon, and back into Alaska. Farther south the Juan de Fuca plate subducts obliquely beneath North America. Notably, to first order, the plate-motion-related active deformation is confined to the coastal and offshore regions of Alaska and British Columbia, and the interior of the Cordillera appears relatively inert (Fig. 1)[10].

Seismicity reported in US and Canadian seismicity catalogues was too sparse to reliably detect any rate changes caused by the Denali earthquake, except in a number of densely monitored volcanic and geothermal areas where triggered seismicity was observed at distances as far as 3,660 km (ref. 8). However, networks of broadband seismographs provided data useful for measuring seismicity rate changes at magnitude levels below regional network detection thresholds. We visually examined approximately 16 hours of broadband data centred temporally on the time of the Denali earthquake at all broadband stations in western Canada and most in the western US. Networks that supplied data include the Canadian National Seismic, the Global Seismic, Pacific Northwest Seismograph, Berkeley Digital Seismic, ANZA Regional and the US National Networks; the Geologic Survey of Canada and the Incorporated Research Institutions for Seismology Data Management System disseminated the data. Whereas the ambient noise and surface waves from the Denali mainshock dominate these data, with frequencies in the 0.2 to 0.02-Hz range, high-pass filtering reveals the higher-frequency signals radiated by small earthquakes local to the recording site (Fig. 2). Unfortunately data retrieval and analysis cannot be automated reliably and are time-consuming; examination of longer time windows is part of ongoing work looking at the duration of the rate increases and their longer-term behaviour.

Although locations cannot be determined from a single recording, the time difference between arriving P and S waves provides estimates of the distance from the station to each earthquake. We only catalogued events with S–P differences of <30 s, corresponding approximately to <240 km, with most events having considerably shorter times and distances. At numerous sites the number of local
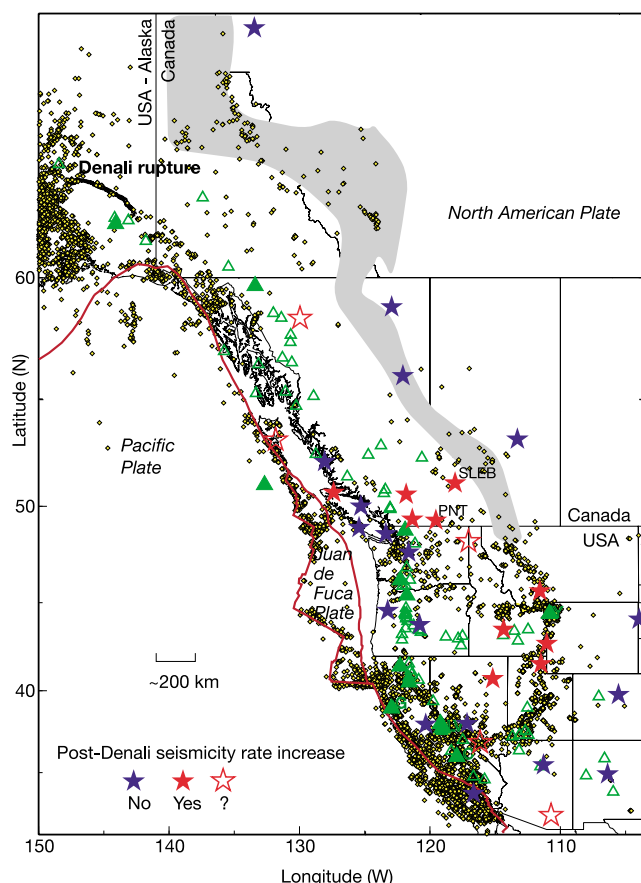
Figure 1 Map of western North America showing the Denali earthquake faults, tectonic features and sites of seismicity rate change observations. Shown are the surface trace of the Denali earthquake rupture (black curve), epicentres of pre-Denali earthquakes with magnitudes >2.0 (yellow dots) for a period of five years before the Denali earthquake (3 November 1997–2002), sites of volcanic activity of the Holocene epoch (open green triangles) and historic age (solid green triangles) (see http://www.volcano.si.edu/world/summinfo.cfm), and broadband seismograph station sites where seismicity rates were examined before and after the Denali earthquake (stars). Star colours indicate whether the seismicity rate increased at the time of the Denali earthquake. Red lines outline plate boundaries. The Pacific–North American boundaries in Canada southward are transform fault zones, the Juan de Fuca–Pacific boundary ridges and transform faults. The Juan de Fuca plate subducts beneath North America, resulting in volcanic chains. The grey band in Canada outlines the 'morphogeologic' transition between deformed strata on the west and flat-lying undeformed strata to the east, or the boundary with stable North America[19]. Geothermal areas where the Denali earthquake triggered seismicity rate increases that are documented elsewhere[8] are not shown.
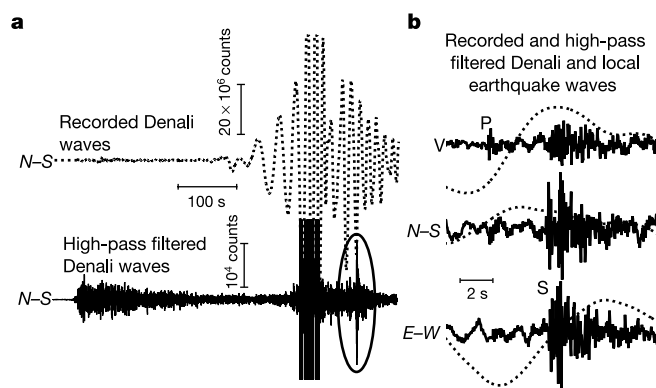
Figure 2 Local earthquake signals revealed in filtered seismograms. **a**, North–south (N–S) component of the Denali mainshock ground velocities (in units of digital counts; dotted trace) at station PNT (Fig. 1) recorded by a broadband seismograph. After filtering out frequencies below ~2 Hz (solid trace) a local earthquake signal (circled) becomes apparent. **b**, Expanded view of the recorded and filtered waveforms within the circled time window on the left, for all three components of ground velocity (V is vertical, E–W is east–west). The arrival times of the P and S waves are clearly observable in the filtered waveforms.

events was significantly greater in the time period after the Denali earthquake than before; at some sites the rate was comparable in the before and after periods, and at others there were only a few local events in the post-Denali period—also indicative of no rate change (Fig. 3). The probability that the latter effect is due instead to a very low background rate (requiring a longer time to see a change) seems low, because similar observations were also made at sites with relatively high background rates. At all triggered sites the first clearly identifiable local, presumably triggered, earthquake occurred within minutes following the arrival of the Denali P wave and after the largest-amplitude surface waves within slower, smaller surface and coda waves (that is, while the Denali signal was above the background noise level). Although seismicity rates fluctuate and may increase in the absence of any obvious external cause, the coincidence of rate-increase onset times near the Denali signal suggests that most, if not all, were not chance occurrences. We also note that in no case was the rate increase delayed from the mainshock signal according to a simple statistical criterion[1], consistent with most observations and theoretical models of aftershocks at near-source distances.

Despite the uneven sampling, the distribution of sites where the seismicity rate increased following the Denali earthquake clearly was not random and extended to distances of 3,385 km from the Denali epicentre, far beyond what is traditionally considered the aftershock region or where permanent stress changes have significant magnitude[1–3] (Fig. 3). As Fig. 1 shows,

the distribution of Denali-triggered sites does not correlate with the regions of highest tectonic loading rates, which should lie close to the plate boundaries and be evident as areas with the greatest ambient seismicity rates[11,12]. Moreover, the locations of triggered seismicity rate increases show no clear correlation with active volcanic or geothermal sites. Particularly striking are the observations in south-central British Columbia. These include triggering at station SLEB, which lies in the foothills of the Canadian Cordillera, almost at the boundary of what is considered to be ancient stable North America, on the basis of geologic and morphologic studies[19]. Just slightly to the west, at station PNT, geodetic studies show that active deformation is 'suspected' but occurs at significantly lower rates than within what is considered the active plate boundary zone[11]—where almost no triggering occurred. A recent analysis of geophysical data in western Canada shows the area of triggered seismicity to be in a transitional zone between old, cold, strong crust to the east and younger, warmer and weaker crust to the west[13]. Our results are consistent with the idea that critically stressed faults may exist nearly anywhere, as inferred from human-induced seismicity, apparently triggered historic earthquakes, and deep drilling studies in intra-plate settings[14–16].

Although there are large gaps in data coverage, Denali triggering plausibly occurs within a continuous band extending from the rupture as far south as northern Utah and Nevada. This band lies approximately on-strike with the Denali fault rupture, which also marks the direction of maximum Love-wave radiation that
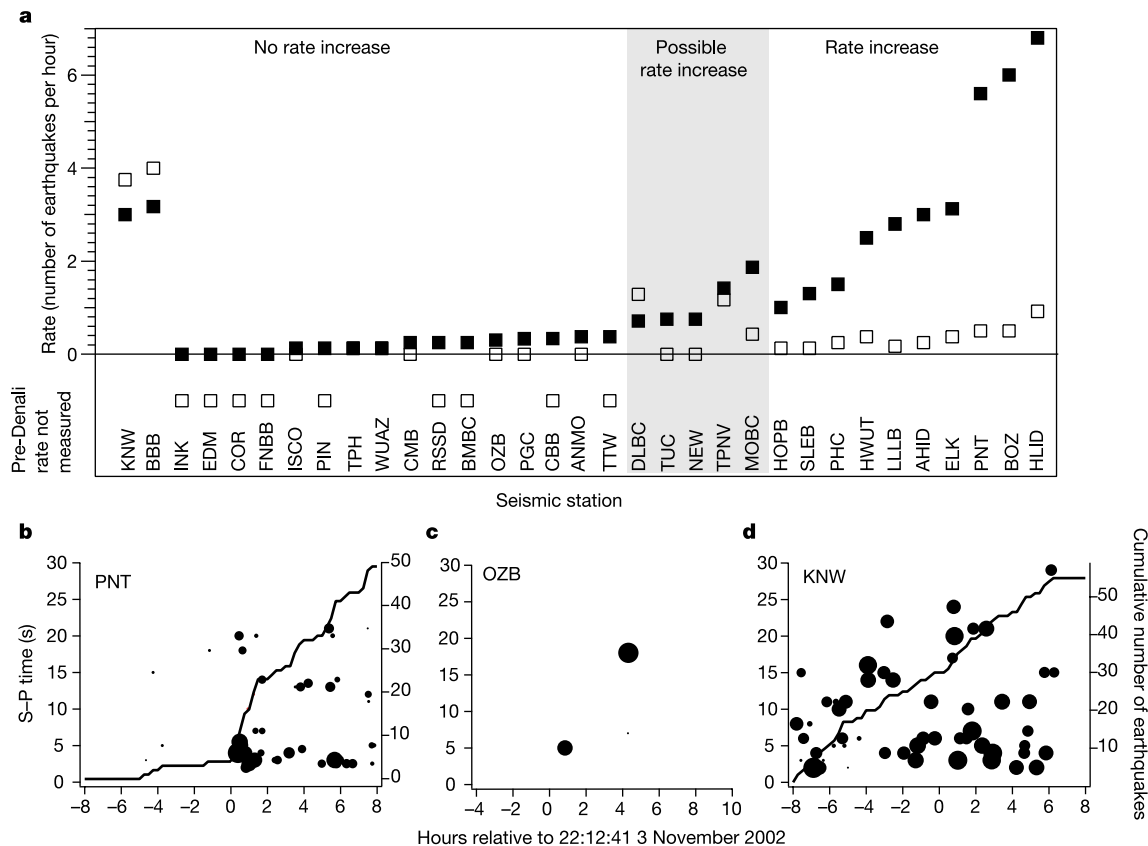

Figure 3 Seismicity rate change observations. **a**, Rates estimated as the number of earthquakes per hour before (open squares) and after (filled squares) the Denali earthquake at each seismic station examined (labelled). At stations where the pre-Denali rate is graphed below zero, no pre-Denali data were examined because the post-Denali rate was insignificant. At the stations where a rate increase was deemed possible but ambiguous (within grey band), the rate increases for a restricted distance (S–P time) range and/or for events bigger than some size limit. **b–d**, Examples of S–P times (left axis, dot

size proportional to log[peak signal amplitude]) of filtered earthquake signals before and after Denali waves arrive. The cumulative pre- and post-Denali earthquake counts (lines) show the rate change or lack of change more clearly. At some sites a post-Denali rate increase is obvious (PNT, Fig. 1), at some the rate does not change (station KNW in southern California), and at others the low post-Denali count implies that either the pre-Denali rate is too low to measure a rate change or that there is none (station OZB on Vancouver Island).
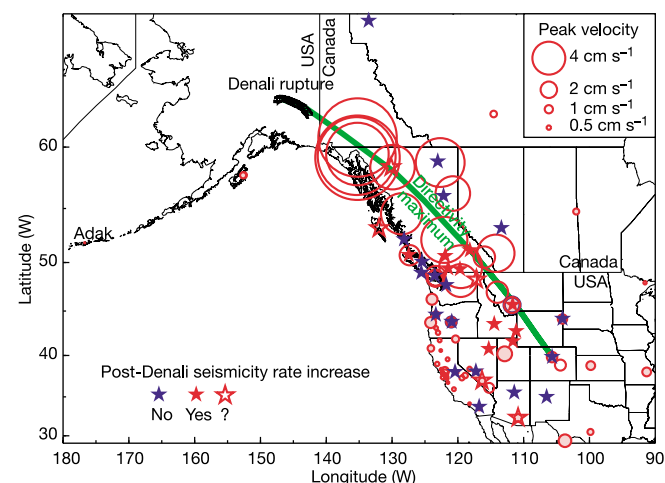
Figure 4 Map of the distributions of Denali-related seismicity rate changes and measured peak Denali seismic ground velocities. The latter are proportional to dynamic strains at these distances[20] and were recorded at broadband seismic stations (shaded circles) and 1-Hz GPS receivers (open circles). Circle centres show locations of recording sites with radii proportional to the measured peak velocity (scale in inset). All measurements in British Columbia and four in the US are from 1-Hz GPS data: note the good agreement with the nearest seismic measurement. The velocities decrease away from the direction of theoretically expected maximum seismic radiation (green segment of a great circle). We label the seismic station at Adak because the measured velocities are too small to be visible. Notably, the sites of triggered rate increases lie roughly within the same azimuthal span as is defined by the maximum measured velocities and theoretically expected dynamic deformations.

dominates the wavefield from a strike–slip earthquake mechanism like the Denali event[8,9]. Moreover, the propagation of the rupture from north to south should focus seismic wave energy along-strike southward of the rupture owing to the focusing phenomena of directivity. We verify these theoretical predictions by mapping the maximum Denali mainshock amplitudes recorded at broadband seismic stations and new permanent GPS receivers that sample at 1 Hz (ref. 17). Canadian GPS data were provided by the Geodetic Survey Division, Geomatics Canada, and Base Mapping and Geomatic Services, British Columbia Ministry of Sustainable Resource Management. Other contributing geodetic networks include the International GPS Service, the Continuously Operating Reference Stations and the University NAVstar Consortium and Aeromap Services. This new application of GPS technology for measuring seismic waves is essential to defining the pattern of seismic radiation, because the Denali seismic waves saturated all the broadband seismographs within British Columbia and most within the most northwestern US.

The combined GPS and seismic data clearly show a focusing of seismic wave energy, or dynamic deformations, consistent with theoretical expectations (Fig. 4). The coincidence of this focusing with the band of triggered seismicity rate increases strongly suggests to us that the dynamic deformations were the triggering agent. However, while this correlation is clearly suggestive, there is not a one-to-one correspondence between the peak amplitude of the dynamic deformation and the change in seismicity rate. This might imply a triggering threshold that depends on tectonic environment[18]. Alternatively or additionally, it might suggest that some other characteristic of the dynamic deformation is important in nucleating rupture (for example, duration or frequency of oscillation). The unprecedented abundance of direct measurements of the dynamic deformation field, albeit at the surface, provides new opportunities to investigate these possibilities. □

1. Hill, D. P. *et al.* Remote seismicity triggered by the M7.5 Landers, California earthquake of June 28, 1992. *Science* **260,** 1617–1623 (1993).
2. Gomberg, J., Beeler, N. & Blanpied, M. On rate-state and Coulomb failure models. *J. Geophys. Res.* **105,** 7857–7872 (2000).
3. Huc, M. & Main, I. G. Anomalous stress diffusion in earthquake triggering: Correlation length, time dependence, and directionality. *J. Geophys. Res.* **108**(B7), doi:10.1029/2001JB001645 (2003).
4. Belardinelli, M. E., Bizzarri, A. & Cocco, M. Earthquake triggering by static and dynamic stress changes. *J. Geophys. Res.* **108**(B3), doi:1029/2002JB001779 (2003).
5. Cocco, M. & Rice, J. R. Pore pressure and poroelasticity effects in Coulomb stress analysis of earthquake interactions. *J. Geophys. Res.* **107**(B2), doi:10.1029/2000JB000138 (2002).
6. Streit, J. E. & Cox, S. F. Fluid pressures at hypocenters of moderate to large earthquakes. *J. Geophys. Res.* **106,** 2235–2243 (2001).
7. Sturtevant, B., Kanamori, H. & Brodsky, E. E. Seismic triggering by rectified diffusion in geothermal systems. *J. Geophys. Res.* **101,** 25269–25282 (1996).
8. Eberhart-Phillips, D. *et al.* The 2002 Denali Fault Earthquake, Alaska: A large magnitude, slip-partitioned event. *Science* **300,** 1113–1118 (2003).
9. Ozacar, A. A., Beck, S. & Christiansen, D. H. Source process of the 3 November 2002 Denali fault earthquake (central Alaska) from teleseismic observations. *Geophys. Res. Lett.* **30,** doi:10.1029/2003GL017272 (2003).
10. Riddihough, R. P. & Hyndman, R. D. in *Geology of the Cordilleran Orogen in Canada* (eds Gabrielse, H. & Yorath, C. J.) Ch. 13, no. 4, 435–455 (Geologic Survey of Canada, Geology of Canada, Ottawa, 1991).
11. Miller, M. M. *et al.* GPS-determination of along-strike variation in Cascadia margin kinematics: Implications for relative plate motion, subduction zone coupling, and permanent deformation. *Tectonics* **20,** 161–176 (2001).
12. Anderson, J. G. *et al.* Seismicity in the western Great Basin apparently triggered by the Landers, California, earthquake 28 June 1992. *Bull. Seismol. Soc. Am.* **84,** 863–891 (1994).
13. Flück, P, Hyndman, R. D. & Lowe, C. Effective elastic thickness Te of the lithosphere in western Canada. *J. Geophys. Res.* **108**(B9), doi:1029/2002JB002201 (2003).
14. Seeber, L., Armbruster, J. G., Kim, W.-Y. & Barstow, N. The 1994 Cacoosing Valley earthquakes near Reading, Pennsylvania:A shallow rupture triggered by quarry unloading. *J. Geophys. Res.* **103,** 24505–24521 (1998).
15. Hough, S. E., Seeber, L. & Armbruster, J. G. Intraplate triggered earthquakes: Observations and interpretation. *Bull. Seismol. Soc. Am.* **93,** 2212–2221 (2003).
16. Townend, J. & Zoback, M. D. How faulting keeps the crust strong. *Geology* **28,** 399–402 (2000).
17. Larson, K., Bodin, P. & Gomberg, J. Using 1 Hz GPS data to measure deformations caused by the Denali fault earthquake. *Science* **300,** 1421–1424 (2003).
18. Gomberg, J., Reasenberg, P., Bodin, P. & Harris, R. Earthquake triggering by transient seismic waves following the Landers and Hector Mine, California earthquakes. *Nature* **411,** 462–466 (2001).
19. Galbrielse, H., Monger, J. W. H., Wheeler, J. O. & Yorath, C. J. in *Geology of the Cordilleran Orogen in Canada* (eds Gabrielse, H. & Yorath, C. J.) Ch. 2, no. 4, 13–59 (Geologic Survey of Canada, Geology of Canada, Ottawa, 1991).
20. Gomberg, J. & Agnew, D. C. The accuracy of seismic estimates of dynamic strains from Pinon Flat Observatory, California, strainmeter and seismograph data. *Bull. Seismol. Soc. Am.* **86,** 212–220 (1996).

Ramp initiation in a thrust wedge

John Panian & David Wiltschko

Department of Geology and Geophysics and Center for Tectonophysics, Texas A&M University, College Station, Texas 77843-3115, USA

Collisional mountain belts are characterized by fold and thrust belts that grow through sequential stacking of thrust sheets from the interior (hinterland) to the exterior (foreland) of the mountain belt[1-5]. Each of these sheets rides on a fault that cuts up through the stratigraphic section on inclined ramps that join a flat basal fault at depth. Although this stair-step or ramp–flat geometry is well known, there is no consensus on why a particular ramp forms where it does. Perturbations in fault shape[6,7], stratigraphy[8,9], fluid pressure[10,11], folding[2,12], and surface slope[13,14] have all been suggested as possible mechanisms. Here we show that such pre-existing inhomogeneities, though feasible causes, are not required. Our computer simulations show that a broad foreland-dipping plastic strain band forms at the surface near the topographic inflection produced by the previous ramp. This